

High-pressure II-III phase transition in solid hydrogen: Insights from state-of-the-art *ab initio* calculations

Maria Hellgren, Damian Contant, Thomas Pitts, and Michele Casula

Sorbonne Université, MNHN, UMR CNRS 7590, IMPMC, 4 place Jussieu, 75005 Paris, France

(Dated: September 13, 2022)

The high-pressure II-III phase transition in solid hydrogen is investigated using the random phase approximation and diffusion Monte Carlo. Good agreement between the methods is found confirming that an accurate treatment of exchange and correlation increases the transition pressure by more than 100 GPa with respect to semilocal density functional approximations. Using an optimized hybrid functional, we then reveal a low-symmetry structure for phase II generated by an out-of-plane librational instability of the C2/c phase III structure. This instability weakens the in-plane polarization of C2/c leading to the well-known experimental signatures of the II-III phase transition such as a sharp shift in vibron frequency, infrared activity and c/a lattice parameter ratio. Finally, we discuss the zero-point vibrational energy that plays an important role in stabilizing phase III at lower pressures.

The phase diagram of pure hydrogen has intrigued and challenged theoretical and experimental physicists for decades. Despite being the simplest element, high-pressure hydrogen forms complex solid phases governed by strongly interacting electrons and quantum nuclei [1–3]. Present knowledge suggests that at low pressure hydrogen consists of freely rotating molecules centered on a hcp structure (phase I). At 110 GPa the Raman roton bands disappear [4, 5] and small vibron discontinuities are observed [6]. This is the onset of the broken symmetry phase (phase II), in which the rotational motion is hindered due to the increasing anisotropic intermolecular interactions, while maintaining strong fluctuating behavior due to the relevance of nuclear quantum effects (NQEs)[7–10]. Around 150 GPa hydrogen enters phase III. The II-III phase transition has been the subject of several studies [11–18]. The transition is detected by the sharp drop of vibron frequency [19, 20], combined with a rapid increase in infrared (IR) activity [6]. The spectral signatures are experimentally well-established and the structures are not expected to largely deviate from the hcp symmetry [21]. However, little is still known concerning the orientational order. Although several structures have been proposed based on theoretical considerations [15, 22–28], large uncertainties remain since their relative energies have been difficult to accurately determine with first-principles calculations. This is mainly due to the approximate treatment of the electron-electron interaction [29–31], but also due to difficulties in including NQEs [32–36].

The most promising candidates for phase III are layered structures, in particular one of C2/c symmetry [37–41], and a more recent one of P6₁22 symmetry [42, 43]. The planar arrangement of the H₂ molecular units induces a polarization and stretches the H₂ bond length. This leads to the strong IR activity and the softened vibron frequency when compared to the many phase II candidate structures, which all contain canted molecules with respect to the hcp planes [15, 28]. Most approxi-

mations within density functional theory (DFT) predict the static (i.e. clamped nuclei) II-III transition to occur below or around the experimental value at about 150-155 GPa [18, 21]. However, more accurate diffusion Monte Carlo (DMC) [30] and coupled cluster single double (CCSD) [31] calculations have shown to shift the static transition pressure beyond 250 GPa. Adding zero-point vibrational energies from DFT to the DMC enthalpies reduces this result by 20 GPa only [30]. These results either questions the structures or suggests that the relative role played by the electron-electron interaction and lattice dynamical effects is not well understood.

In this work, we reexamine the II-III phase transition in solid hydrogen using state-of-the-art *ab initio* calculations based on the random phase approximation (RPA) and DMC. We discover a new low-symmetry structure for phase II that is stabilized by nuclear vibrations and, unlike previous candidate structures, emerges from a continuous symmetry breaking of phase III. This rationalizes several experimental outcomes. Furthermore, we show that the transition pressure is compatible with experimental findings when accurate electronic energies are considered, together with zero-point energy variations. We finally provide an estimate of NQEs, in terms of quantum anharmonicity across the transition.

Many previous works have applied DMC to hydrogen, and it provides the gold standard for this system [29, 30, 44, 45]. Here, we use DMC in its lattice regularized version [46] to project an initial variational wave function of Jastrow-Slater form, with Slater orbitals generated by DFT within the local density approximation. Further details can be found in the supplemental material (SM) [47].

The RPA is known for high accuracy at moderate computational cost [48–50], and is here applied to hydrogen for the first time. It combines exact exchange with a formally exact expression for the correlation energy E_c written in terms of the dynamical linear density response

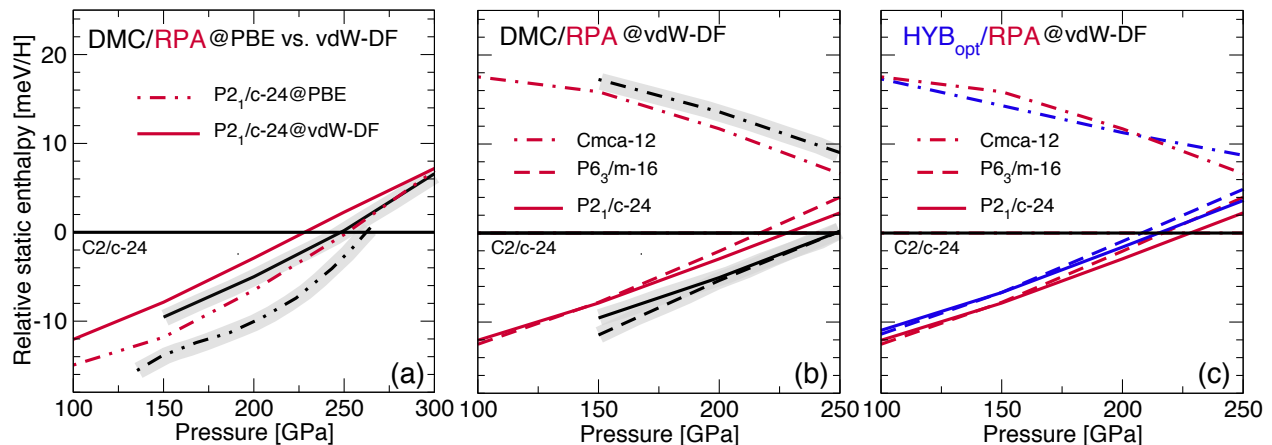


Figure 1. RPA (red) compared to DMC (black, (a) and (b)) and HYB_{opt} (blue, (c)). The @DFT notation refers to the DFT approximation used to optimise the geometry at fixed pressure. The $\text{P2}_1/\text{c-24@PBE}$ result is extracted from Ref. [30]. The DMC error bars are indicated by a gray shaded area, having a height of ± 0.9 meV, around the mean values.

function χ_λ

$$E_c = - \int_0^1 d\lambda \int_0^\infty \frac{d\omega}{2\pi} \text{Tr} \{v[\chi_\lambda(i\omega) - \chi_s(i\omega)]\}. \quad (1)$$

Within the RPA $\chi_\lambda(i\omega)$ fulfills the time-dependent Hartree equations: $\chi_\lambda(i\omega) = \chi_s(i\omega) + \chi_s(i\omega)\lambda v\chi_\lambda(i\omega)$, where $\chi_s(i\omega)$ is the independent-particle Kohn-Sham response function and v is the Coulomb interaction. Including a vertex via the exact-exchange kernel leads to the RPA with exchange (RPAX), which has proven to give more reliable energy differences due to systematically improved total energies [51–56]. Here, we will use the RPAX, not only as an additional validation of the RPA, but also to optimize the fraction of exchange in an approximate hybrid functional.

We start by demonstrating the performance of RPA in the 100-300 GPa pressure range. We study several structures previously proposed in the literature (denoted by their symmetry and number of atoms); $\text{P2}_1/\text{c-24}$, $\text{P6}_3/\text{m-16}$ and $\text{Pca2}_1\text{-8}$ for phase II and $\text{C2}/\text{c-24}$ and Cmca-12 for phase III. Within a given symmetry the geometry is optimized using the vdW-DF functional [57]. Previous calculations have shown that this functional gives accurate geometries at fixed volume for molecular solid hydrogen [29]. In Fig. 1(a) we report the results for the static enthalpy difference between $\text{P2}_1/\text{c-24}$ and $\text{C2}/\text{c-24}$ with DMC and RPA, as well as the result from an earlier DMC calculation that used structures optimized with PBE [30]. For comparison, RPA results obtained on PBE structures are also presented [58]. First of all, we see that the shift in transition pressure due to the change of functional used to optimize the geometry is of the order 20 GPa with both DMC and RPA. Secondly, RPA is found to be in very good agreement with DMC, staying consistently within 2 meV/H around the DMC mean value over the whole pressure range.

In panel 1(b), $\text{P6}_3/\text{m-16}$ and Cmca-12 are also included. A recent CCSD calculation of static enthalpies predicted the phase II candidate $\text{P6}_3/\text{m-16}$ to be the most stable phase up to 350 GPa [31]. Our DMC calculation contradicts this result, with $\text{P6}_3/\text{m-16}$ being degenerate with $\text{P2}_1/\text{c-24}$ within error bars (± 0.9 meV). This behaviour is also confirmed by our RPA calculation, and it is independent of the theory used to optimize the geometry. There is also a good agreement between DMC and RPA for the Cmca-12 structure. Cmca-12 was originally a candidate for phase III but is now expected to become important at higher pressures, close to the insulator-to-metal transition [38–41, 44, 45, 59].

We have also carried out RPAX calculations on the same structures. Including exchange in the response function has a very small effect on the RPA energy differences in these systems, as shown in the SM [47]. Thus, the agreement between RPA, RPAX and DMC provides strong confirmation that the static II-III transition pressure, with the currently known structures, should lie at about 225-250 GPa, irrespective of whether $\text{P2}_1/\text{c-24}$ or $\text{P6}_3/\text{m-16}$ is used for phase II. We will later show that, according to our most accurate calculations, a third competing symmetry for phase II, i.e. $\text{Pca2}_1\text{-8}$, lies very close in energy to the other two phases. These results imply an overestimation of 70-100 GPa with respect to experiment. This is also independent of whether $\text{C2}/\text{c-24}$ or $\text{P6}_1\text{22-36}$ is used for phase III. Indeed, they can be considered degenerate within the DMC error bars in the pressure range analyzed here (see SM). However, we chose $\text{C2}/\text{c-24}$ as a reference structure for phase III in what follows.

To investigate the reason for the difference with respect to experiment and to include effects of lattice vibrations, we now analyse the possibility of using a hybrid functional that retains the QMC and RPA accuracy at a cheaper cost. The standard PBE0 functional with 25%

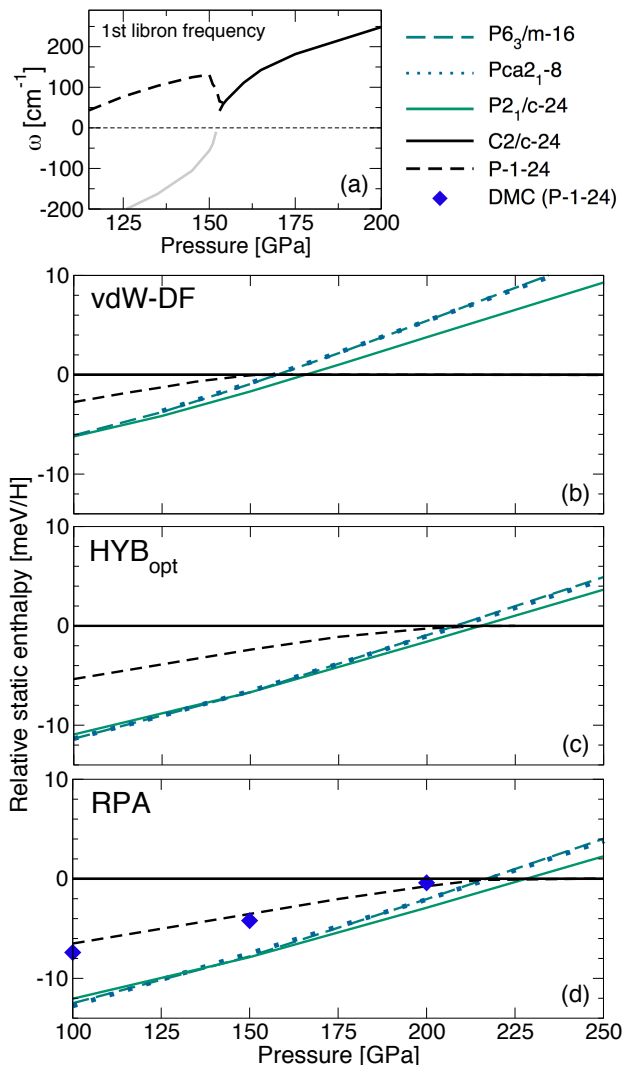


Figure 2. The frequency of the unstable vdW-DF libron as a function of pressure is shown in (a), with the imaginary frequency (grey) shown as a negative frequency. Relative static enthalpy of P2₁/c-24, P6₃/m-16 and Pca2₁-8 with respect to C2/c-24 for (b) vdW-DF, (c) HYB_{opt} and (d) RPA. The enthalpy of the structure obtained by following the librational instability of C2/c-24 is also displayed and denoted P-1-24. The DMC results for P-1-24 are marked with blue diamonds in panel (d). Their size spans the range covered by the DMC error bars.

of exchange does not improve the enthalpy differences with respect to semilocal DFT functionals (see SM [47]). However, exact-exchange is clearly of crucial importance in the molecular phases of solid hydrogen since PBE and Hartree-Fock alone give II-III transition pressures at 110 GPa and beyond 450 GPa, respectively [31]. We will, therefore, optimize a new fraction of exchange using the accurate RPax total energy. The optimization is carried out by minimizing the RPax total energy of an isolated H₂ molecule with respect to the fraction of exchange used

to generate the input density [60, 61]. The approach is described in Ref. [56] and in the SM [47]. We find a minimum at 48%, which is well beyond the standard value. The results from this optimized hybrid functional, which we denote as HYB_{opt}, are presented in Fig. 1 (c). The good agreement with RPA shows that a hybrid functional with a carefully chosen exact-exchange fraction is sufficient to produce accurate enthalpies.

We can now use HYB_{opt} to study the stability of the structures and the impact of their relaxed geometry [62]. Comparing enthalpy differences using vdW-DF and HYB_{opt} geometries gives a difference of less than 1 meV/H. The static enthalpy differences that we have obtained with vdW-DF geometries are thus robust to further variations in the geometry. The stability of the structures can then be studied by calculating the vibrational spectra. With HYB_{opt} we are limited to Γ -point vibrations, but with vdW-DF we can study dense \mathbf{q} -point grids. We found P2₁/c-24 and P6₃/m-16 to both be stable with vdW-DF in the pressure range investigated. Interestingly, C2/c-24 is found to have Γ -instabilities (two nearly degenerate imaginary phonons) below 215 GPa with HYB_{opt} and below 150 GPa with vdW-DF, i.e. exactly at the expected static II-III transition within the given functional. The lowest vdW-DF libron that becomes imaginary is shown as a function of pressure in Fig. 2 (a). We note that a similar behaviour has been observed by Raman spectroscopy [5, 14, 63, 64], suggesting the onset of a libron instability within phase III, in proximity to the transition pressure. The unstable libron mode generates a new structure with lower symmetry, in which two thirds of the C2/c-24 molecules are rotated out of plane (the structures are visualized in the SM [47]). The space-group symmetry is thereby reduced to P-1, i.e., only inversion symmetry remains. By displacing the atoms in C2/c-24 according to the phonon mode eigenvector, we find a symmetric double-well potential. However, the minimum of this potential is strongly underestimated since the molecular tilting should be accompanied

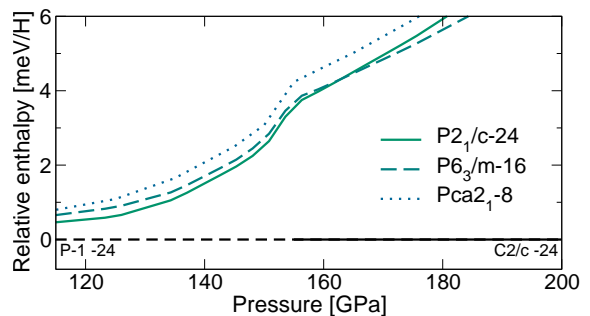


Figure 3. Relative enthalpies within vdW-DF including ZPEs in the harmonic approximation. The ZPE of P-1-24 is smaller than the ZPE of P2₁/c-24, P6₃/m-16 and Pca2₁-8, reversing their order of stability.

by an H_2 bond length contraction and an expansion of the c/a lattice parameter ratio. Indeed, after a full geometry relaxation, the energy gain increases by two orders of magnitude. Using our HYB_{opt} optimized geometries, the lowering of energy is confirmed at both the RPA and DMC level (Fig. 2(d)).

In Fig. 2 we summarize the results for the phase diagram with clamped nuclei, including also the stable $Pca2_1-8$ phase II structure. Comparing DMC, RPA, HYB_{opt} and vdW-DF a clear trend emerges. The position of the instability in $C2/c-24$ coincides with the transition between $C2/c-24$ and all the proposed phase II structures, which are all nearly degenerate, independently of which functional is used. Furthermore, all approximations predict the $P-1-24$ structure to lie above the phase II candidates. Therefore, $P-1-24$ does not appear competitive at any pressure. However, this picture changes when we consider lattice vibrations.

Let us now include lattice dynamics via the harmonic zero-point vibrational energy (ZPE). Due to the presence of the $C2/c-24$ instability, it is necessary to use the same functional for the electronic energy as for generating the structures and computing the ZPEs. Previous calculations used PBE structures, where such an instability occurs below the range of interest (at 110 GPa) [30]. Calculating the ZPE with RPA and HYB_{opt} is presently not feasible due to the high computational cost of using supercells. However, we can consistently include the ZPE within the cheaper vdW-DF functional [65]. The result can be found in Fig. 3. We immediately see that the corresponding picture is different. The phase II candidates are all shifted by roughly the same amount, falling above the $C2/c-24$ and $P-1-24$ structures. Below 150 GPa, $P-1-24$ is now the most stable. Given the similarity in qualitative behaviour between the different functionals, it is plausible that we would find the same ordering of enthalpies with the more advanced electronic structure methods.

Having shown that $P-1-24$ is a promising candidate for phase II, let us move to an in-depth analysis of the transition. A well-established experimental feature of the II-III phase transition is the sharp shift of 80 cm^{-1} in vibron frequency [19–21, 59]. In Fig. 4 we plot the lowest vibron frequency, which is Raman active, as a function of pressure. The left panel (a) shows the vdW-DF results for $C2/c-24$, $P2_1/c-24$, $P6_3/m-16$ and $Pca2_1-8$ and the right panel (b) shows the HYB_{opt} results for $C2/c-24$ and $P2_1/c-24$. The change of $C2/c-24$ into $P-1-24$ is marked by dashed lines. At 155 GPa, i.e. at the transition to $P-1-24$, the $C2/c-24$ vdW-DF vibron exhibits a continuous but sharp increase, whose size is very similar to the experimental result marked in red [20]. There is an overall difference of approximately 400 cm^{-1} with respect to experiment that can only be accounted for when calculating the vibrations beyond the harmonic approximation [41, 66]. We note that the frequency shift going

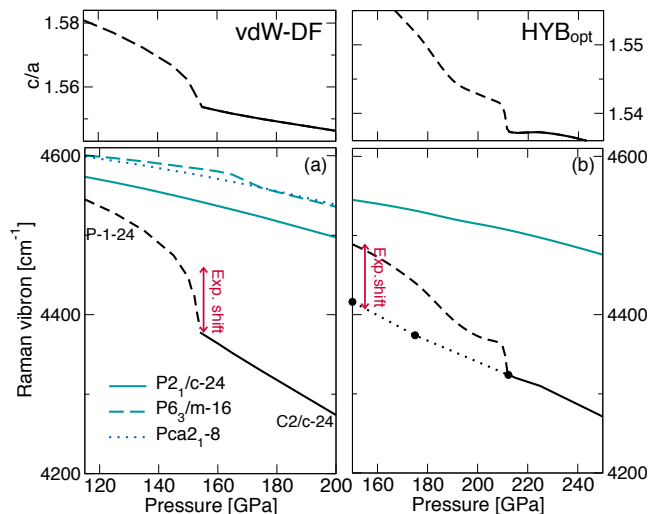


Figure 4. (a) The lowest vibron frequency as a function of pressure within vdW-DF for $P2_1/c-24$, $P6_3/m-16$, $Pca2_1-8$ and $C2/c-24$. A rapid upshift in the frequency is observed at the transition from $C2/c-24$ (full line) to $P-1-24$ (dashed line). A similar shift is seen in the c/a ratio, as shown in the upper panel. (b) The same results with HYB_{opt} for $P2_1/c-24$ and $C2/c-24$. Black dots joined by the dotted line correspond to the frequencies obtained from the unstable $C2/c-24$ structure. The experimental shift of 80 cm^{-1} at 155 GPa [20] is marked in both panels (vertically upshifted with respect to experiment).

from $C2/c-24$ to $P-1-24$ agrees better with experiment than going from $C2/c-24$ to any of the other candidate phase II structures. We expect effects of anharmonicity to mostly cancel but any effect would most likely increase the shift since the $C2/c-24$ vibron is more anharmonic due to the stronger in-plane interactions. The HYB_{opt} result is qualitatively similar to the vdW-DF result, although the vibron shift appears sharper and is smaller than with vdW-DF. However, when extrapolated to 155 GPa using the unstable $C2/c-24$ structure (i.e. when calculated at the experimental transition pressure) the shift again agrees well with experiment.

So far, $C2/c-24$ has only been challenged by the similar $P6_122-36$ structure [42, 43]. To show that the mechanism we found is common to these phase-III type of structures, we have repeated the calculations above for $P6_122-36$. Indeed, the vibron shift is almost identical and caused by a librational instability very similar to the one in $C2/c-24$. The results can be found in the SM [47]. One could reasonably assume that other energetically competitive planar structures, if found for example by structural searches using a functional beyond PBE, are likely to exhibit the same feature.

The cause of the abrupt change in vibron frequency is related to the shortening of the intramolecular bond lengths in $P-1-24$. Indeed, the out-of-plane rotation of the H_2 units weakens the in-plane intermolecular inter-

actions that stretch the bond length. At the same time, the c -parameter of the nearly hexagonal lattice abruptly increases. In the upper panels of Fig. 4 (a) and (b) we have plotted the c/a lattice parameter ratio as a function of pressure. We observe a shift very similar to the one in vibron frequency [67]. This behaviour has also been observed by X-ray diffraction [21]. In addition, by studying the charge distribution, we find that the polarization of some of the molecules reduces by a factor of two when rotated out of plane (see SM [47] for a Bader analysis [68, 69] of the charges in C2/ c -24 and P-1-24). This change is reflected in the IR activity, which rapidly decreases moving from phase III to phase II [6]. In the SM we present the IR intensity as a function of pressure using the vdW-DF functional. A qualitatively good agreement with experiment is found.

Let us finally discuss the vibrational contribution to the P-1-24 to C2/ c -24 transition pressure. The exact calculation of the transition pressure, including all effects of vibrations, represents a very difficult task. Indeed, the electron-electron interaction should be described at least at the level of a hybrid functional and lattice vibrations should be calculated beyond the harmonic approximation. However, we can make an initial estimate by calculating the variation in the harmonic ZPE due to the change in vibrons only. The 12 vibrons are only weakly \mathbf{k} -dependent so we can make the estimate at the Γ -point. We find that the P-1-24 energy increases by around 2 meV/H with both vdW-DF and HYB_{opt}. This would already lower the transition pressure by 40 GPa. Moreover, quantum anharmonicity strongly affects the orientational symmetry breaking of the molecular in-plane order. Indeed, the instability driven by the lowest librational modes can be modelled by a double well potential, as previously mentioned. According to this simple model, derived from HYB_{opt} energies, NQEs reduce the transition pressure by an additional amount of 20 GPa, due to quantum resymmetrization effects (see SM) [70]. A very mild isotope effect is found, in accordance with experiments [16, 71]. This brings the transition pressure obtained with the most advanced electronic structure methods to a value much closer to experiment, corroborating the mechanism of the transition.

In conclusion, using a combination of RPA, DMC, hybrid DFT and vdW-DF functionals, we have provided new insights into the nature of the II-III phase transition. We have revealed the existence of a libron instability in C2/ c -24 that generates a new broken symmetry phase when the pressure is lowered, in which two thirds of the H₂ molecules are rotated out of plane. This relatively small orientational change is sufficient to quantitatively reproduce the experimental signatures of a sharp vibron shift and an order of magnitude increase of IR intensity, at the pressure where the system undergoes the transition into phase III.

The work was performed using HPC resources

from GENCI-TGCC/CINES/IDRIS (Grants No. A0110907625 and A0110906493). Financial support from Emergence-Ville de Paris is acknowledged. This work was partially supported by the European Centre of Excellence in Exascale Computing TREX-Targeting Real Chemical Accuracy at the Exascale, funded by the European Union’s Horizon 2020 Research and Innovation program under Grant Agreement No. 952165.

-
- [1] Isaac F. Silvera, “The solid molecular hydrogens in the condensed phase: Fundamentals and static properties,” *Rev. Mod. Phys.* **52**, 393–452 (1980).
 - [2] Ho-kwang Mao and Russell J Hemley, “Ultrahigh-pressure transitions in solid hydrogen,” *Reviews of modern physics* **66**, 671 (1994).
 - [3] Jeffrey M. McMahon, Miguel A. Morales, Carlo Pierleoni, and David M. Ceperley, “The properties of hydrogen and helium under extreme conditions,” *Rev. Mod. Phys.* **84**, 1607–1653 (2012).
 - [4] Hector E. Lorenzana, Isaac F. Silvera, and Kenneth A. Goettel, “Orientational phase transitions in hydrogen at megabar pressures,” *Phys. Rev. Lett.* **64**, 1939–1942 (1990).
 - [5] Alexander F. Goncharov, Russell J. Hemley, Ho-kwang Mao, and Jinfu Shu, “New high-pressure excitations in parahydrogen,” *Phys. Rev. Lett.* **80**, 101–104 (1998).
 - [6] Michael Hanfland, Russell J. Hemley, and Ho-kwang Mao, “Novel infrared vibron absorption in solid hydrogen at megabar pressures,” *Phys. Rev. Lett.* **70**, 3760–3763 (1993).
 - [7] S Biermann, D Hohl, and D Marx, “Quantum effects in solid hydrogen at ultra-high pressure,” *Solid state communications* **108**, 337–341 (1998).
 - [8] Grégory Geneste, Marc Torrent, Francois Bottin, and Paul Loubeyre, “Strong isotope effect in phase II of dense solid hydrogen and deuterium,” *Physical Review Letters* **109**, 155303 (2012).
 - [9] Yanier Crespo, Alessandro Laio, Giuseppe E. Santoro, and Erio Tosatti, “Theory of the reentrant quantum rotational phase transition in high-pressure HD,” *Phys. Rev. B* **84**, 144119 (2011).
 - [10] Michael P. Surh, K. J. Runge, T. W. Barbee, E. L. Pollock, and C. Mailhot, “Ab initio calculations for solid molecular hydrogen,” *Phys. Rev. B* **55**, 11330–11341 (1997).
 - [11] Russell J Hemley, Zoltan G Soos, Michael Hanfland, and Ho-kwang Mao, “Charge-transfer states in dense hydrogen,” *Nature* **369**, 384–387 (1994).
 - [12] I.I. Mazin and R. E. Cohen, “Insulator-metal transition in solid hydrogen: Implication of electronic-structure calculations for recent experiments,” *Physical Review B* **52**, R8597 (1995).
 - [13] Lijing Cui, Nancy H Chen, and Isaac F Silvera, “Excitations, order parameters, and phase diagram of solid deuterium at megabar pressures,” *Physical Review B* **51**, 14987 (1995).
 - [14] I. I. Mazin, R. J. Hemley, A. F. Goncharov, Michael Hanfland, and Ho-kwang Mao, “Quantum and classical orientational ordering in solid hydrogen,” *Physical review*

- letters **78**, 1066 (1997).
- [15] Jorge Kohanoff, Sandro Scandolo, Stefano de Gironcoli, and Erio Tosatti, “Dipole-quadrupole interactions and the nature of phase III of compressed hydrogen,” *Phys. Rev. Lett.* **83**, 4097–4100 (1999).
- [16] B Edwards and NW Ashcroft, “Order in dense hydrogen at low temperatures,” *Proceedings of the National Academy of Sciences* **101**, 4013–4018 (2004).
- [17] Pierre Tolédano, Hannelore Katzke, Alexander F Goncharov, and Russell J Hemley, “Symmetry breaking in dense solid hydrogen: Mechanisms for the transitions to phase II and phase III,” *Physical review letters* **103**, 105301 (2009).
- [18] Alexander F. Goncharov, Russell J. Hemley, and Hengkang Mao, “Vibron frequencies of solid H₂ and D₂ to 200 GPa and implications for the P-T phase diagram,” *The Journal of Chemical Physics* **134**, 174501 (2011).
- [19] R. J. Hemley and H. K. Mao, “Phase transition in solid molecular hydrogen at ultrahigh pressures,” *Phys. Rev. Lett.* **61**, 857–860 (1988).
- [20] Hector E. Lorenzana, Isaac F. Silvera, and Kenneth A. Goettel, “Evidence for a structural phase transition in solid hydrogen at megabar pressures,” *Phys. Rev. Lett.* **63**, 2080–2083 (1989).
- [21] Yuichi Akahama, Manabu Nishimura, Haruki Kawamura, Naohisa Hirao, Yasuo Ohishi, and Kenichi Takekura, “Evidence from X-ray diffraction of orientational ordering in phase III of solid hydrogen at pressures up to 183 GPa,” *Phys. Rev. B* **82**, 060101(R) (2010).
- [22] Hubert M. James, “Orientational order in solid ortho-hydrogen. II. hexagonal close-packed molecular lattice,” *Phys. Rev.* **167**, 862–874 (1968).
- [23] Hitose Nagara and Tuto Nakamura, “Stable phases of solid hydrogen at megabar pressures and at zero temperature,” *Phys. Rev. Lett.* **68**, 2468–2471 (1992).
- [24] Vincent Natoli, Richard M Martin, and David Ceperley, “Crystal structure of molecular hydrogen at high pressure,” *Physical review letters* **74**, 1601 (1995).
- [25] Jorge Kohanoff, Sandro Scandolo, Guido L Chiarotti, and Erio Tosatti, “Solid molecular hydrogen: The broken symmetry phase,” *Physical review letters* **78**, 2783 (1997).
- [26] Kurt A Johnson and NW Ashcroft, “Structure and bandgap closure in dense hydrogen,” *Nature* **403**, 632–635 (2000).
- [27] “Structure and spectroscopic properties of dense solid hydrogen at 160 GPa,” *Solid State Communications* **145**, 5–10 (2008).
- [28] Vanessa Labet, Roald Hoffmann, and N. W. Ashcroft, “A fresh look at dense hydrogen under pressure. III. two competing effects and the resulting intra-molecular H-H separation in solid hydrogen under pressure,” *The Journal of Chemical Physics* **136**, 074503 (2012).
- [29] Raymond C. Clay, Jeremy Mcminis, Jeffrey M. McMahon, Carlo Pierleoni, David M. Ceperley, and Miguel A. Morales, “Benchmarking exchange-correlation functionals for hydrogen at high pressures using quantum Monte Carlo,” *Phys. Rev. B* **89**, 184106 (2014).
- [30] Neil D Drummond, Bartomeu Monserrat, Jonathan H Lloyd-Williams, P López Ríos, Chris J Pickard, and Richard James Needs, “Quantum Monte Carlo study of the phase diagram of solid molecular hydrogen at extreme pressures,” *Nature communications* **6**, 1–6 (2015).
- [31] Ke Liao, Xin-Zheng Li, Ali Alavi, and Andreas Grüneis, “A comparative study using state-of-the-art electronic structure theories on solid hydrogen phases under high pressures,” *npj Computational Materials* **5**, 1–6 (2019).
- [32] Bartomeu Monserrat, N. D. Drummond, and R. J. Needs, “Anharmonic vibrational properties in periodic systems: energy, electron-phonon coupling, and stress,” *Phys. Rev. B* **87**, 144302 (2013).
- [33] Sam Azadi, N. D. Drummond, and W. M. C. Foulkes, “Nature of the metallization transition in solid hydrogen,” *Physical Review B* **95**, 035142 (2017).
- [34] Giovanni Rillo, Miguel A. Morales, David M. Ceperley, and Carlo Pierleoni, “Coupled electron-ion Monte Carlo simulation of hydrogen molecular crystals,” *The Journal of Chemical Physics* **148**, 102314 (2018).
- [35] Lorenzo Monacelli, Raffaello Bianco, Marco Cherubini, Matteo Calandra, Ion Errea, and Francesco Mauri, “The stochastic self-consistent harmonic approximation: calculating vibrational properties of materials with full quantum and anharmonic effects,” *Journal of Physics: Condensed Matter* **33**, 363001 (2021).
- [36] T. Morresi, L. Paulatto, R. Vuilleumier, and M. Casula, “Probing anharmonic phonons by quantum correlators: A path integral approach,” *The Journal of Chemical Physics* **154**, 224108 (2021).
- [37] Chris J Pickard and Richard J Needs, “Structure of phase III of solid hydrogen,” *Nature Physics* **3**, 473–476 (2007).
- [38] M. I. Eremets, A. P. Drozdov, P. P. Kong, and H. Wang, “Semimetallic molecular hydrogen at pressure above 350 GPa,” *Nature Physics* (2019), 10.1038/s41567-019-0646-x.
- [39] Paul Loubeyre, Florent Occelli, and Paul Dumas, “Synchrotron infrared spectroscopic evidence of the probable transition to metal hydrogen,” *Nature* **577**, 631–635 (2020).
- [40] Vitaly Gorelov, Markus Holzmann, David M. Ceperley, and Carlo Pierleoni, “Energy gap closure of crystalline molecular hydrogen with pressure,” *Phys. Rev. Lett.* **124**, 116401 (2020).
- [41] Lorenzo Monacelli, Ion Errea, Matteo Calandra, and Francesco Mauri, “Black metal hydrogen above 360 GPa driven by proton quantum fluctuations,” *Nature Physics* (2020), 10.1038/s41567-020-1009-3.
- [42] Bartomeu Monserrat, Richard J. Needs, Eugene Gregoryanz, and Chris J. Pickard, “Hexagonal structure of phase III of solid hydrogen,” *Phys. Rev. B* **94**, 134101 (2016).
- [43] Sam Azadi and Thomas D. Kühne, “Unconventional phase III of high-pressure solid hydrogen,” *Phys. Rev. B* **100**, 155103 (2019).
- [44] Jeremy McMinis, Raymond C. Clay, Donghwa Lee, and Miguel A. Morales, “Molecular to atomic phase transition in hydrogen under high pressure,” *Physical Review Letters* **114**, 105305 (2015).
- [45] Lorenzo Monacelli, Michele Casula, Kosuke Nakano, Sandro Sorella, and Francesco Mauri, “Quantum phase diagram of high-pressure hydrogen,” *arXiv preprint arXiv:2202.05740* (2022).
- [46] Michele Casula, Claudia Filippi, and Sandro Sorella, “Diffusion Monte Carlo method with lattice regularization,” *Physical review letters* **95**, 100201 (2005).
- [47] See Supplemental Materials at [URL will be inserted by publisher] for additional information about the computational details, structural visualization, a complementary analysis of the P6₁22-36 structure, the nuclear quantum

- effects analysis across the II-III phase transition, Bader charge analysis and infrared spectra [31, 46, 72–76].
- [48] Xinguo Ren, Patrick Rinke, Christian Joas, and Matthias Scheffler, “Random-phase approximation and its applications in computational chemistry and materials science,” *Journal of Materials Science* **47**, 7447–7471 (2012).
- [49] Huy-Viet Nguyen and Stefano de Gironcoli, “Efficient calculation of exact exchange and RPA correlation energies in the adiabatic-connection fluctuation-dissipation theory,” *Phys. Rev. B* **79**, 205114 (2009).
- [50] Judith Harl and Georg Kresse, “Accurate bulk properties from approximate many-body techniques,” *Phys. Rev. Lett.* **103**, 056401 (2009).
- [51] Maria Hellgren and Ulf von Barth, “Correlation energy functional and potential from time-dependent exact-exchange theory,” *The Journal of Chemical Physics* **132**, 044101 (2010).
- [52] Andreas Heßelmann and Andreas Görling, “Random phase approximation correlation energies with exact Kohn-Sham exchange,” *Molecular Physics* **108**, 359–372 (2010).
- [53] Nicola Colonna, Maria Hellgren, and Stefano de Gironcoli, “Correlation energy within exact-exchange adiabatic connection fluctuation-dissipation theory: Systematic development and simple approximations,” *Phys. Rev. B* **90**, 125150 (2014).
- [54] Patrick Bleiziffer, Marcel Krug, and Andreas Görling, “Self-consistent kohn-sham method based on the adiabatic-connection fluctuation-dissipation theorem and the exact-exchange kernel,” *The Journal of Chemical Physics* **142**, 244108 (2015).
- [55] Maria Hellgren, Nicola Colonna, and Stefano de Gironcoli, “Beyond the random phase approximation with a local exchange vertex,” *Phys. Rev. B* **98**, 045117 (2018).
- [56] Maria Hellgren and Lucas Baguet, “Random phase approximation with exchange for an accurate description of crystalline polymorphism,” *Phys. Rev. Research* **3**, 033263 (2021).
- [57] M. Dion, H. Rydberg, E. Schröder, D. C. Langreth, and B. I. Lundqvist, “Van der Waals density functional for general geometries,” *Phys. Rev. Lett.* **92**, 246401 (2004).
- [58] All calculations are done with the Quantum ESPRESSO package [77] using an ONCV (Optimized Norm-Conserving Vanderbilt) pseudopotential [78]. More details can be found in the SM.
- [59] Paul Loubeyre, Florent Occelli, and René LeToullec, “Optical studies of solid hydrogen to 320 GPa and evidence for black hydrogen,” *Nature* **416**, 613–617 (2002).
- [60] Maria Hellgren, Lucas Baguet, Matteo Calandra, Francesco Mauri, and Ludger Wirtz, “Electronic structure of TiSe₂ from a quasi-self-consistent G_0W_0 approach,” *Phys. Rev. B* **103**, 075101 (2021).
- [61] Ngoc Linh Nguyen, Nicola Colonna, and Stefano de Gironcoli, “Ab initio self-consistent total-energy calculations within the EXX/RPA formalism,” *Phys. Rev. B* **90**, 045138 (2014).
- [62] Structural relaxation with hybrid functionals was performed using the VASP code [79–81].
- [63] R. J. Hemley, H. K. Mao, and J. F. Shu, “Low-frequency vibrational dynamics and structure of hydrogen at megabar pressures,” *Physical review letters* **65**, 2670 (1990).
- [64] Alexander F Goncharov, Eugene Gregoryanz, Russell J Hemley, and Ho-kwang Mao, “Spectroscopic studies of the vibrational and electronic properties of solid hydrogen to 285 GPa,” *Proceedings of the National Academy of Sciences* **98**, 14234–14237 (2001).
- [65] Zero-point energies are calculated using density functional perturbation theory as implemented within the QE PHonon code [77, 82].
- [66] Tommaso Morresi, Rodolphe Vuilleumier, and Michele Casula, “Hydrogen phase-iv characterization by full account of quantum anharmonicity,” *Phys. Rev. B* **106**, 054109 (2022).
- [67] Hikaru Kitamura, Shinji Tsuneyuki, Tadashi Ogitsu, and Takashi Miyake, “Quantum distribution of protons in solid molecular hydrogen at megabar pressures,” *Nature* **404**, 259–262 (2000).
- [68] Richard F. W. Bader, “A quantum theory of molecular structure and its applications,” *Chemical Reviews* **91**, 893–928 (1991).
- [69] G. Henkelman, A. Arnaldsson, and H. Jonsson, “A fast and robust algorithm for bader decomposition of charge density,” *Comput. Mater. Sci.* **36**, 354–360 (2006).
- [70] Ion Errea, Matteo Calandra, Chris J. Pickard, Joseph R. Nelson, Richard J. Needs, Yinwei Li, Hanyu Liu, Yunwei Zhang, Yanming Ma, and Francesco Mauri, “Quantum hydrogen-bond symmetrization in the superconducting hydrogen sulfide system,” *Nature* **532**, 81–84 (2016).
- [71] A. F. Goncharov, I. I. Mazin, J. H. Eggert, R. J. Hemley, and Ho-kwang Mao, “Invariant points and phase transitions in deuterium at megabar pressures,” *Physical review letters* **75**, 2514 (1995).
- [72] Kousuke Nakano, Claudio Attaccalite, Matteo Barborini, Luca Capriotti, Michele Casula, Emanuele Coccia, Mario Dagrada, Claudio Genovese, Ye Luo, Guglielmo Mazzola, *et al.*, “TurboRVB: A many-body toolkit for ab initio electronic simulations by quantum Monte Carlo,” *The Journal of Chemical Physics* **152**, 204121 (2020).
- [73] Sorella Sorella, Nicolas Devaux, Mario Dagrada, Guglielmo Mazzola, and Michele Casula, “Geminal embedding scheme for optimal atomic basis set construction in correlated calculations,” *The Journal of chemical physics* **143**, 244112 (2015).
- [74] CJ Umrigar, Julien Toulouse, Claudia Filippi, Sandro Sorella, and Richard G Hennig, “Alleviation of the fermion-sign problem by optimization of many-body wave functions,” *Physical review letters* **98**, 110201 (2007).
- [75] M. Calandra Buonauro and S. Sorella, “Numerical study of the two-dimensional Heisenberg model using a Green function Monte Carlo technique with a fixed number of walkers,” *Physical Review B* **57**, 11446 (1998).
- [76] Hendra Kwee, Shiwei Zhang, and Henry Krakauer, “Finite-size correction in many-body electronic structure calculations,” *Physical review letters* **100**, 126404 (2008).
- [77] P. Giannozzi *et al.*, “Advanced capabilities for materials modeling with Quantum ESPRESSO,” *J. Phys.: Condens. Matter* **29**, 465901 (2017).
- [78] D. R. Hamann, “Optimized norm-conserving Vanderbilt pseudopotentials,” *Physical Review B* **88** (2013), 10.1103/physrevb.88.085117.
- [79] G. Kresse and J. Furthmüller, “Efficient iterative schemes for ab initio total-energy calculations using a plane-wave basis set,” *Phys. Rev. B* **54**, 11169 (1996).
- [80] G. Kresse and J. Furthmüller, “Efficiency of ab-initio total energy calculations for metals and semiconductors us-

ing a plane-wave basis set,” *Comput. Mater. Sci.* **6**, 15 (1996).

[81] G. Kresse and D. Joubert, “From ultrasoft pseudopotentials to the projector augmented-wave method,” *Phys.*

Rev. B **59**, 1758 (1999).

[82] Stefano Baroni, Stefano de Gironcoli, Andrea Dal Corso, and Paolo Giannozzi, “Phonons and related crystal properties from density-functional perturbation theory,” *Rev. Mod. Phys.* **73**, 515–562 (2001).

SUPPLEMENTAL MATERIALS FOR: HIGH-PRESSURE II-III PHASE TRANSITION IN SOLID HYDROGEN: INSIGHTS FROM STATE-OF-THE-ART *AB INITIO* CALCULATIONS

Below we present additional information about the computational details, structural visualization, a complementary analysis of the P6₁22-36 structure, the nuclear quantum effects analysis across the II-III phase transition, Bader charge analysis and infrared spectra.

QMC CALCULATIONS DETAILS

Diffusion Monte Carlo (DMC) calculations have been performed using the lattice regularized DMC scheme (LRDMC) [46], as implemented in the TurboRVB package [72]. DMC allows one to access properties of the quantum many-body distribution that is obtained by projecting the initial variational wave function toward the ground state of the system within the fixed-node (FN) approximation.

To initialize the many-body state, we employed a Jastrow-Slater variational wave function $\Psi^{\mathbf{k}}(\mathbf{R}) = \exp\{-U(\mathbf{R})\} \det\{\phi_j^{\mathbf{k}}(\mathbf{r}_i^{\uparrow})\} \det\{\phi_j^{\mathbf{k}}(\mathbf{r}_i^{\downarrow})\}$ for $i, j \in \{1, \dots, N/2\}$, where N is the number of electrons in the unpolarized supercell, \mathbf{k} is the twist belonging to a Monkhorst-Pack (MP) grid of the supercell Brillouin zone, and $\mathbf{R} = \{\mathbf{r}_1^{\uparrow}, \dots, \mathbf{r}_{N/2}^{\uparrow}, \mathbf{r}_1^{\downarrow}, \dots, \mathbf{r}_{N/2}^{\downarrow}\}$ is the N -electron coordinate.

U is the Jastrow function, split into three contributions: $U = U_{en} + U_{ee} + U_{een}$. The electron-nucleus function U_{en} has an exponential decay and is given by $U_{en} = \sum_{iI} J_{1b}(r_{iI}) + U_{en}^{\text{no-cusp}}$, where the index $i(I)$ runs over electrons (nucleus), r_{iI} is the electron-nucleus distance, and $J_{1b}(r) = \alpha(1 - \exp\{-r/\alpha\})$, with a variational parameter α . J_{1b} cures the nuclear cusp conditions, and allows the use of the bare Coulomb potential in our QMC framework. The electron-electron function U_{ee} has a Padé form and is given by $U_{ee} = -\sum_{i \neq j} J_{2b}(r_{ij})$, where the indices i and j run over electrons, r_{ij} is the electron-electron distance, and $J_{2b}(r) = 0.5r/(1 + \beta r)$, with a variational parameter β . This two-body Jastrow term fulfills the cusp conditions for antiparallel electrons. The last term in the Jastrow factor is the electron-electron-nucleus function: $U_{een} = \sum_{(i \neq j)I} \sum_{\gamma\delta} M_{\gamma\delta I} \chi_{\gamma I}(r_{iI}) \chi_{\delta I}(r_{jI})$, with $M_{\gamma\delta I}$ a matrix of variational parameters, and $\chi_{\gamma I}(r)$ a $(2s, 2p, 1d)$ Gaussian basis set, with orbital index γ , centered on the nucleus I . Analogously, the electron-nucleus cusp-free contribution to the Jastrow function, $U_{en}^{\text{no-cusp}}$, is developed on the same Gaussian basis set, such that $U_{en}^{\text{no-cusp}} = \sum_{iI} \sum_{\gamma} V_{\gamma I} \chi_{\gamma I}(r_{iI})$, where $V_{\gamma I}$ is a vector of parameters. The J_{1b} and J_{2b} Jastrow functions are made periodic using a $\mathbf{r} \rightarrow \mathbf{r}'$ mapping that makes the distances diverge at the border of the unit cell, as explained in Ref. [72]. For the inhomogeneous U_{een} part and for the electron-nucleus term $U_{en}^{\text{no-cusp}}$, the Gaussian basis set χ is made periodic by summing over replicas translated by lattice vectors.

The one-body orbitals ϕ are expanded in a primitive $(4s, 2p, 1d)$ Gaussian basis set, which we contracted into 6 hybrid orbitals using the geminal embedding orbitals (GEO) contraction scheme [73] at the Γ point. The ϕ orbitals are made periodic using the same scheme as for the χ orbitals. This basis set yields a FN-LRDMC bias in the energy differences smaller than the target error of 1 meV per atom. For each \mathbf{k} belonging to the MP grid of a given supercell (see Tab. I), we performed independent DFT calculations in the local density approximation (LDA) to generate $\{\phi_j^{\mathbf{k}}\}_{j=1, \dots, N/2}$ for all occupied states. These LDA calculations are done for the fully *ab initio* Hamiltonian with bare Coulomb potential for the electron-ion interactions. The same Hamiltonian is then solved using LRDMC.

Before running LRDMC calculations, we optimized the α , β , $M_{\gamma\delta I}$ and $V_{\gamma I}$ parameters, keeping the orbitals $\phi_i^{\mathbf{k}}$ fixed. These parameters are optimized by minimizing the variational energy of the wave function Ψ within the QMC linear optimization method [74]. All \mathbf{k} -twists share the same Jastrow factor. The LRDMC projection is carried out at the lattice space $a = 0.25a_0$, where a_0 is the Bohr radius, yielding converged energy differences. For example, in Fig. 5 we show the lattice space extrapolation of the total energy for the C2/ c and the P2₁/ c symmetries, computed at 150 GPa, as well as the lattice space extrapolation of their energy difference. As one can see, energy differences are converged in lattice space already for larger values of a than the one used in this work. This is an advantage with respect to the “standard” diffusion Monte Carlo algorithm, which sometimes has a less smooth convergence in

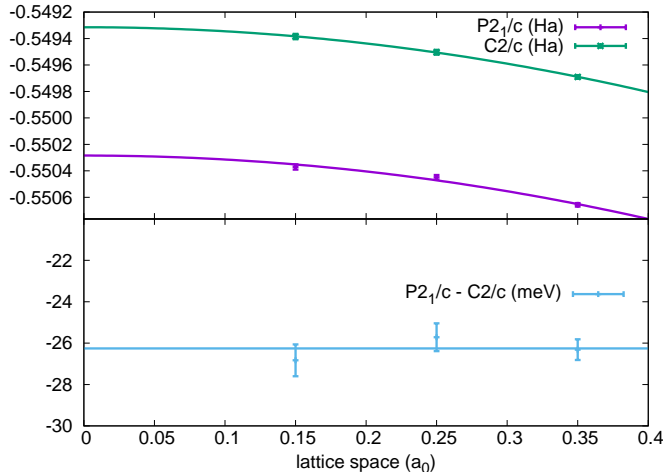


Figure 5. Lattice space convergence of LRDMC total energies for the P2₁/c and C2/c structures at a volume corresponding to 150 GPa. Upper panel: total energies extrapolations in Hartree/H. Lower panel: constant extrapolation of the energy difference in meV/H. In energy differences, convergence is reached already at $a = 0.35a_0$.

the time step. Indeed, in LRDMC the lattice space extrapolation has an a^2 behavior, which is given by the lattice regularization of the kinetic term.

For LRDMC equilibration, we discarded the first 5 blocks from the averages of each twist, to get rid of the transient regime. A single block is made of 25 branching steps, each step is made of 100 moves on the LRDMC random lattice. This corresponds to an imaginary time evolution of 0.43 Ha^{-1} per branching step. The time propagation for each twist is carried by 32 walkers, within a fixed walker population algorithm. This is enough for a stable projection, given the quality of our starting variational wave function. The finite size population bias has been removed by the “correcting factors scheme” [75]. This sampling strategy allows us to reach a target statistical precision of about 1 meV/H, once the statistics is gathered from all \mathbf{k} -twists used.

crystal symmetry	\mathbf{k} -mesh size	supercell size	N
C2/c-24	$6 \times 12 \times 6$	$2 \times 1 \times 2$	96
P-1-24	$6 \times 12 \times 6$	$2 \times 1 \times 2$	96
Cmca-12	$6 \times 6 \times 6$	$2 \times 2 \times 2$	96
P2 ₁ /c-24	$12 \times 6 \times 6$	$1 \times 2 \times 2$	96
P6 ₃ /m-16	$6 \times 6 \times 6$	$2 \times 2 \times 2$	128

Table I. \mathbf{k} -meshes and supercell sizes employed in our QMC simulations of crystal symmetries shown in the first column. The last column reports the number of atoms N in the corresponding supercell. \mathbf{k} -meshes are expressed with respect to the supercell Brillouin zone.

In our QMC calculations, we used \mathbf{k} -meshes and supercell sizes reported in Tab. I. To further reduce finite-size errors, we used Kwee-Zhang-Krakauer (KZK) corrected energies [76]. The KZK corrections as a function of pressure and crystal symmetry are reported in Tab. II for the smallest supercell size taken into account in the present work. As one can see, the KZK correction dependence on the specific crystal symmetry at fixed pressure and fixed size is negligible within 1 meV/H accuracy. Therefore, KZK corrections largely cancel out in the energy differences at the given pressure, if the supercell size is the same.

We ran all LRDMC calculations long enough to reach a statistical error of about 1 meV per atom ($\pm 0.9 \text{ meV/H}$ for $N=96$). For the systems and pressures studied here, this computational setup leads to systematic finite-size errors whose magnitude falls into the statistical error bar.

To check for the presence of a finite-size bias, we performed additional calculations with a larger supercell, $N=288$, for C2/c, P2₁/c and P6₃/m at pressures of 150 GPa and 200 GPa, and compare with the results obtained from smaller systems. The results are reported in Tab. III, where “regular supercell” is the one with at least 96 atoms, used throughout the paper, while “large supercell” is the one with 288 atoms. As it is apparent from the Table, the ΔE

crystal symmetry	150 GPa	200 GPa	250 GPa	300 GPa
C2/c-24 ($N=96$)	91.7	97.5	102.0	105.9
P2 ₁ /c-24 ($N=96$)	91.5	97.0	101.6	105.5
Cmca-12 ($N=96$)	92.0	97.6	102.2	106.1
P6 ₃ /m-16 ($N=128$)	68.4	72.6	76.0	78.9

Table II. Magnitude of KZK corrections for the pressures analyzed, and for different structures at the smallest supercell size taken into account in the present work (reported in parenthesis). The numerical entries are in meV/H.

systems	supercell size	ΔE (meV/H)	$\sigma_{\Delta E}$ (meV/H)	large/regular variation in units of σ
P2 ₁ /c - C2/c (150 GPa)	regular	-9.5	0.7	
P2 ₁ /c - C2/c (150 GPa)	large	-8.2	1.2	1.0
P2 ₁ /c - C2/c (200 GPa)	regular	-5.0	0.7	
P2 ₁ /c - C2/c (200 GPa)	large	-7.1	1.2	-1.5
P6 ₃ /m - C2/c (150 GPa)	regular	-11.4	0.9	
P6 ₃ /m - C2/c (150 GPa)	large	-7.8	1.3	2.3
P6 ₃ /m - C2/c (200 GPa)	regular	-5.3	0.8	
P6 ₃ /m - C2/c (200 GPa)	large	-4.2	1.3	0.7

Table III. Energy difference fluctuations due to the change of supercell size. The variation is reported in statistical error (σ) units in the last column.

variation between the two sizes falls within 2 standard deviations in absolute value. Thus, the residual FS bias, if present, is of the order of the statistical error bar.

To compute enthalpies from internal energies, we employed the pressures estimated at the HYB_{opt} level. We checked that these pressures are in statistical agreement with the QMC pressures, which have however an error bar of ≈ 2 GPa on average. Therefore, to keep the error bar on the final enthalpies small, we used the HYB_{opt} pressures in the transformation.

DETAILS OF THE DFT AND RPA CALCULATIONS

Density functional calculations based on PBE and vdW-DF have been performed with Quantum ESPRESSO (QE) [77] and an ONCV (Optimized Norm-Conserving Vanderbilt) pseudopotential [78]. For structural optimization we used 110 Ry plane-wave cutoff and up to $8 \times 8 \times 8$ \mathbf{k} -point grids. Zero point energies were calculated using density functional perturbation theory as implemented within the PHonon package. Hybrid functional calculations were performed with QE on vdW-DF and PBE geometries. The volume was optimized by minimizing the hybrid enthalpy at fixed pressure. The relative enthalpies of P2₁/c-24 and P6₃/m-16 with respect to C2/c-24 on PBE geometries can be found in Fig. 6, including also the CCSD results of Ref. [31] and the DMC results obtained in this work.

Full structural optimization using hybrid functionals was carried out with the VASP code [79–81] using the PAW method and 400 eV plane-wave cutoff. The charge density for the Bader analysis [68, 69] was also obtained with the VASP code using the vdW-DF functional.

The RPA and RPax calculations were performed using an implementation based on an eigenvalue decomposition of the response function [49, 53, 56]. For the correlation energies we used a plane-wave cutoff energy of 60 Ry and 8 eigenvalues per electron for the response function. The convergence with respect to these two parameters can be found in Fig. 3. The \mathbf{k} -points were converged at $5 \times 3 \times 5$ (C2/c-24), $2 \times 7 \times 2$ (P2₁/c-24), $5 \times 5 \times 6$ (P6₃/m-16), $5 \times 8 \times 6$ (Pca2₁-8) and $4 \times 4 \times 4$ (Cmca-12). In RPax we used smaller grids to save computational cost [$4 \times 3 \times 4$ (C2/c-24), $3 \times 4 \times 3$ (P2₁/c-24), $4 \times 4 \times 4$ (P6₃/m-16), and $4 \times 4 \times 4$ (Cmca-12)] but staying within 2 meV of accuracy. In Fig. 7 we present a comparison between RPA and RPax.

The α -parameter of the hybrid functional is optimized by numerically minimizing the total energy in RPax with respect to the α used to generate the input density, i.e.

$$\frac{dE^{\text{RPax}}[n^\alpha]}{d\alpha} = 0. \quad (2)$$

The local xc potential of the hybrid functional needed to generate n^α is defined as the functional derivative of the

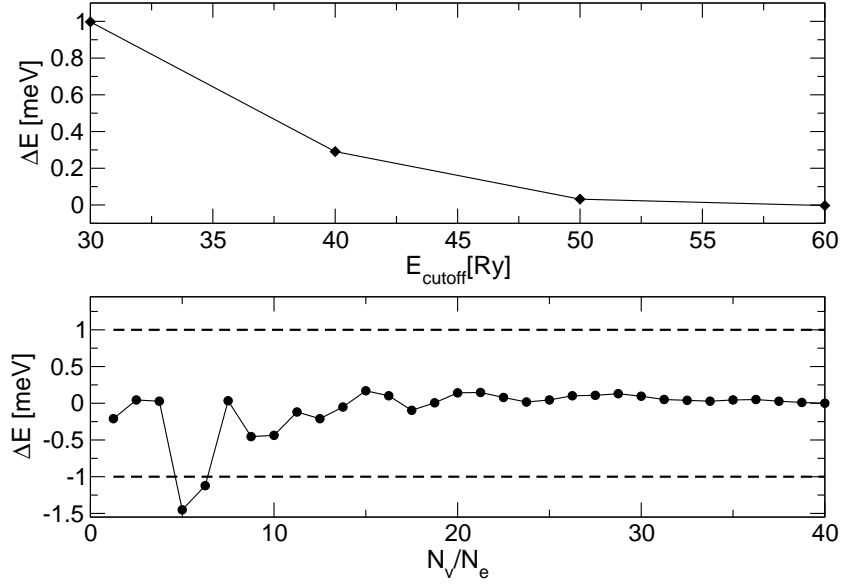


Figure 6. Convergence of the plane-wave cutoff energy (top) and the number of eigenvalues used in the response function (bottom) in the RPA calculations.

hybrid xc energy with respect to the density. It can thus be decomposed into [60]

$$v_{\text{xc}}^{\text{hyb},\alpha} = v_{\text{x}}^{\alpha} + (1 - \alpha)v_{\text{x}}^{\text{PBE}} + v_{\text{c}}^{\text{PBE}}. \quad (3)$$

For the exchange part, an integral equation known as the linearized Sham-Schlüter equation has to be solved

$$\int d2 \chi_s(1, 2)v_{\text{x}}^{\alpha}(2) = -i\alpha \int d2d3 G_s(3, 1)G_s(1, 2)\Sigma_s^{\text{HF}}(2, 3) \quad (4)$$

where Σ_s^{HF} is the Fock self-energy, G_s is the Kohn-Sham Green's function and χ_s is the Kohn-Sham independent particle response function. This equation is solved using an iterative technique as described in Ref. [61]. The result for an isolated H_2 molecule is presented in Fig. 8.

The RPA/RPax energies were evaluated on top of PBE orbitals. We have verified that using orbitals from a local hybrid potential with an optimal fraction of exchange does not change the energy differences significantly.

THE II-III TRANSITION PRESSURE WITH VARIOUS APPROXIMATIONS TO THE EXCHANGE AND CORRELATION ENERGY

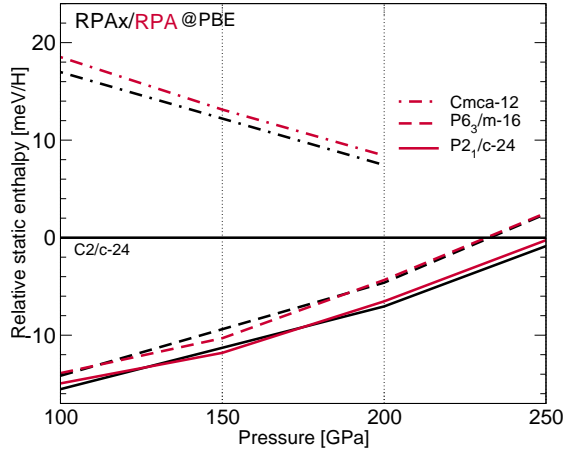


Figure 7. RPAX compared to RPA.

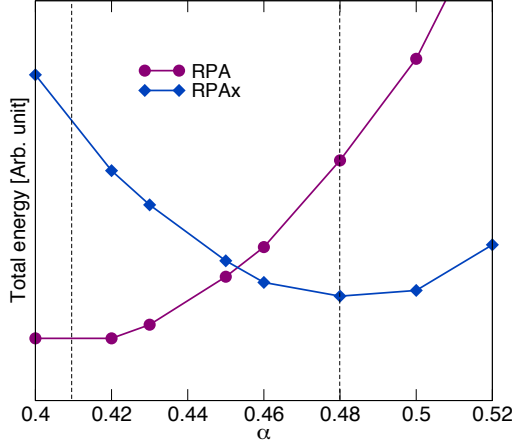


Figure 8. The α -parameter of the hybrid functional is determined by locating the minimum of the RPAX total energy on the H_2 molecule.

THE C2/C-24 AND P-1-24 STRUCTURES

ANALYSIS OF THE P6₁22-36 SYMMETRY

With the aim at quantifying the relative stability between the P6₁22-36 structure and the C2/c-24 one in the 150-250 GPa pressure range, we carried out additional extensive QMC calculations at 150 GPa. According to Ref. [43], at this pressure the energy difference between these two phases should be maximized and in favor of P6₁22 by at least 17 meV/H. We performed LRDMC simulations up to a system size of 432 atoms, with \mathbf{k} -points sampling (corresponding to a $12 \times 12 \times 12$ Monkhorst-Pack grid for the unit cell) and KZK 2-body corrections, and we found that the C2/c and P6₁22 are nearly degenerate in enthalpy, with a small 2.5 ± 1.1 meV gain for the C2/c structure. With the reached QMC statistical accuracy, they can be considered as degenerate within two error bars. The finite-size extrapolation is plotted in Fig. 11 for both phases, showing the DMC total enthalpies for the sizes we computed in order to resolve their energy difference in the thermodynamic limit. The largest evaluated size, $N=432$, corresponds to a $2 \times 2 \times 3$ supercell for the P6₁22 crystal symmetry. The above result is in agreement with HYB_{opt} calculations that we performed in addition to our QMC results. This outcome is at variance with Ref. [43], which instead reports the P6₁22 structure as the most stable one. We attribute the source of this discrepancy to a too coarse \mathbf{k} -mesh employed in that work. Nevertheless, the two structures stay very close to each other in enthalpy, and a possible polymorphism of phase III in this pressure range, favored by nuclear quantum effects (NQEs), is likely.

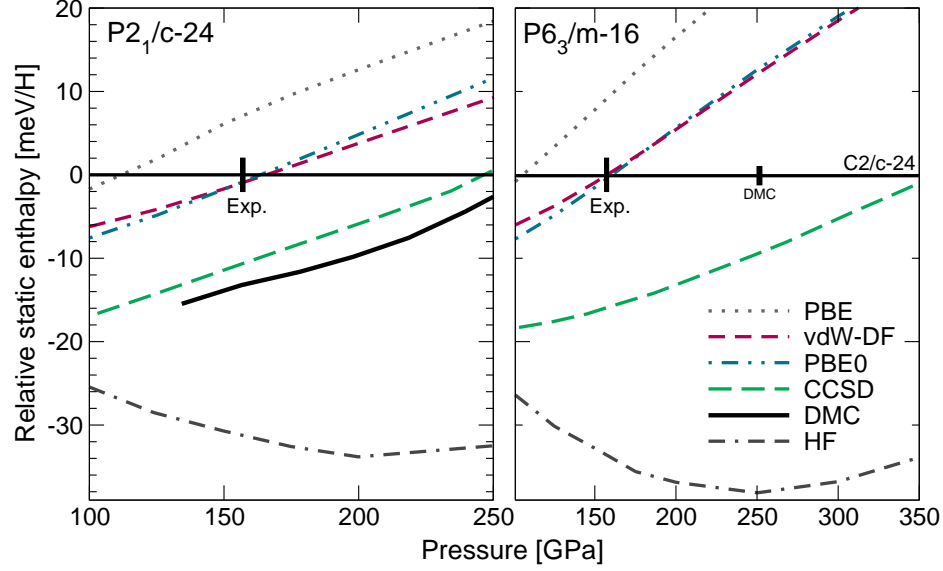


Figure 9. The II-III transition pressure with various approximations to the exchange and correlation energy (PBE, vdW-DF, PBE0, CCSD, DMC and HF).

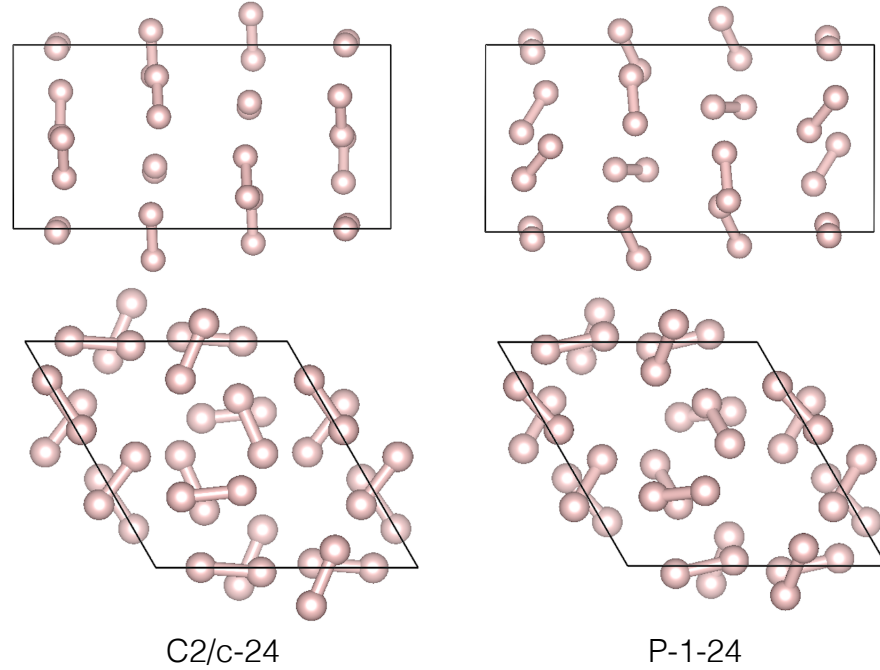


Figure 10. View along the c -axis (top) and the a -axis (bottom) of $C2/c-24$ (left) and $P-1-24$ (right).

Since the $P6_122$ structure is very similar to $C2/c$, one would expect similar structural instabilities that can explain the II-III transition. As shown in Fig. 12, we have verified that the $P6_122$ has a libron instability similar to the one of $C2/c$, giving rise to a vibron jump with the same magnitude. The only difference with respect to $C2/c$ is that it

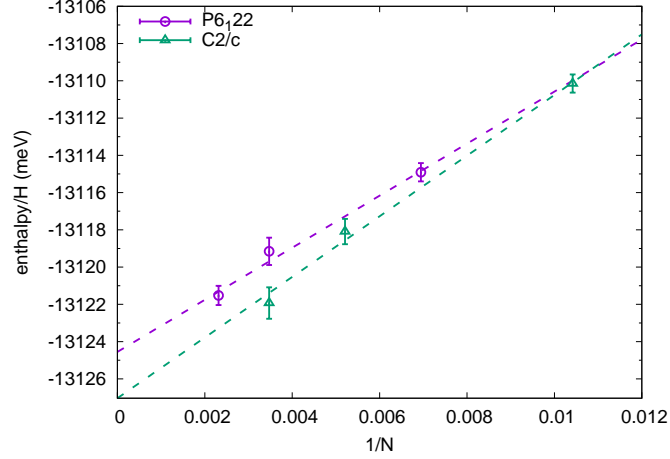


Figure 11. Total enthalpies of $P6_122$ and $C2/c$ structures, for different system sizes. For $C2/c$, we considered the $2 \times 1 \times 2$, $2 \times 2 \times 2$, and $2 \times 3 \times 2$ supercells, while for $P6_122$ we computed the $2 \times 2 \times 1$, $2 \times 2 \times 2$ and $2 \times 2 \times 3$ supercells. The largest one computed has $N=432$ hydrogen atoms. The dashed lines indicate the extrapolated enthalpies.

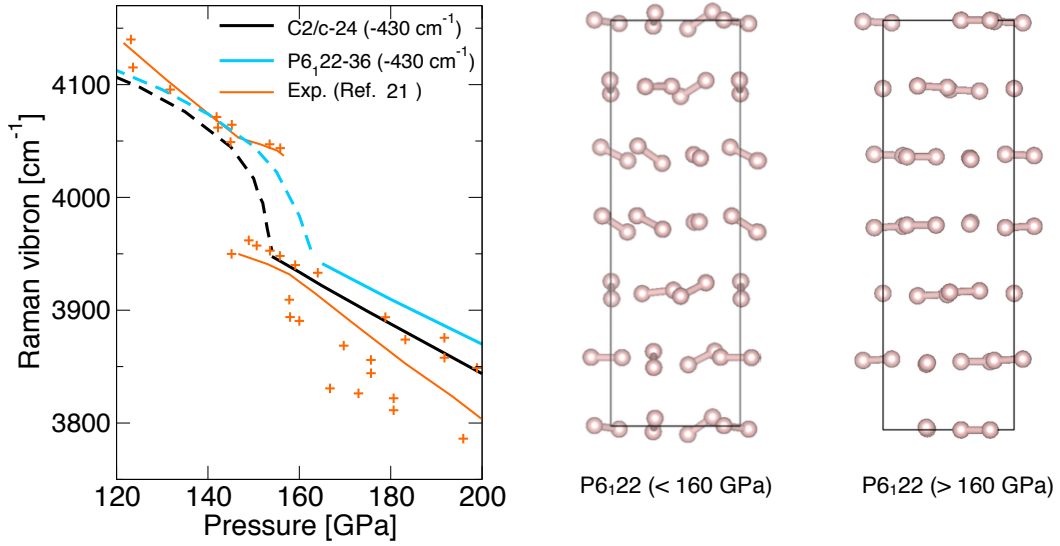


Figure 12. Left: The first vibron frequency as a function of pressure for the $C2/c-24$ and $P6_122-36$ structures. A symmetry lowering occurs at 155 GPa and 160 GPa respectively, marked by dashed lines. The theoretical results are shifted by -430 cm^{-1} (a value close to the expected anharmonic shift) in order to compare the frequency shift at the transition with experiment (here taken from Ref. [20]). Right: Structure of $P6_122-36$ along the c -axis below and above the transition (visualized at 140 GPa).

occurs at a slightly larger pressure (by 5 GPa).

NUCLEAR QUANTUM EFFECTS ACROSS THE II-III PHASE BOUNDARY

In order to estimate the NQEs across the II-III phase boundary, we modeled the total energy E of the system (unit cell) as a function of the scalar order parameter h by using a Landau-like potential whose form is

$$E(h) = a + bh^2 + ch^4. \quad (5)$$

We take the order parameter h as the distance between the hydrogen atoms belonging to the canted (out-of-plane) H_2 molecules and the hcp layer of the H_2 centers of mass. While a is an irrelevant energy shift, b and c are determined by the equilibrium value h_{\min} of the order parameter, i.e. the canted equilibrium geometry, and by the energy gain Δ of the P-1-24 phase with respect to the $C2/c$ symmetry of phase III. Straightforwardly, $b = -2\Delta/h_{\min}^2$ and $c = \Delta/h_{\min}^4$. Thus, both b and c are pressure (p) dependent through the p dependence of h and Δ . The symmetry of the potential in Eq. 5 is dictated by the fact that the P-1-24 crystalline symmetry allows for two degenerate equilibrium geometries (given by h_{\min} and $-h_{\min}$), and the broken order parameter h_{\min} continuously goes to zero as $p \rightarrow p_c$, with p_c the critical pressure of the II-III phase transition.

To include NQEs, we solve the one-dimensional Schrödinger equation

$$\left(-\frac{1}{2M}\nabla_h^2 + E(h)\right)\Psi = E\Psi, \quad (6)$$

where M is the effective mass given by $M = 0.5N_{\text{mol}}m_{H/D}$, with N_{mol} the number of canted molecules in the unit cell, $m_{H/D}$ the proton/deuterium mass in Hartree units, and 0.5 the reduced mass of a single H_2 molecule. If the resulting ground state (GS) wave function $\Psi = \Psi(h)$ of Eq. 6 is bimodal, then the system is in the broken phase II. If Ψ has a peak at $h = 0$, namely if the average molecular distribution is an in-plane configuration, the system is in phase III.

The results reported in Fig. . for both hydrogen (upper row) and deuterium (lower row), are obtained using a potential derived from *ab initio* HYB_{opt} geometries and energies. One can notice that, according to the model in Eq. 6, the transition (shown in the central panels) takes place at $p_c \in [190 - 198]$ GPa ($p_c \in [198 - 204]$ GPa) for hydrogen (deuterium), at variance with the “static lattice” system, where the transition happens at ≈ 220 GPa, as yielded by our advanced calculations (HYB_{opt}, many-body RPA and QMC, see main text). The pressure range depends on the number N_{mol} of canted molecules taken into account in the model. Indeed, as shown in Figs. 6 and 7, not all out-of-plane molecules share the same h in the 12- H_2 unit cell. It is possible to distinguish three groups, made

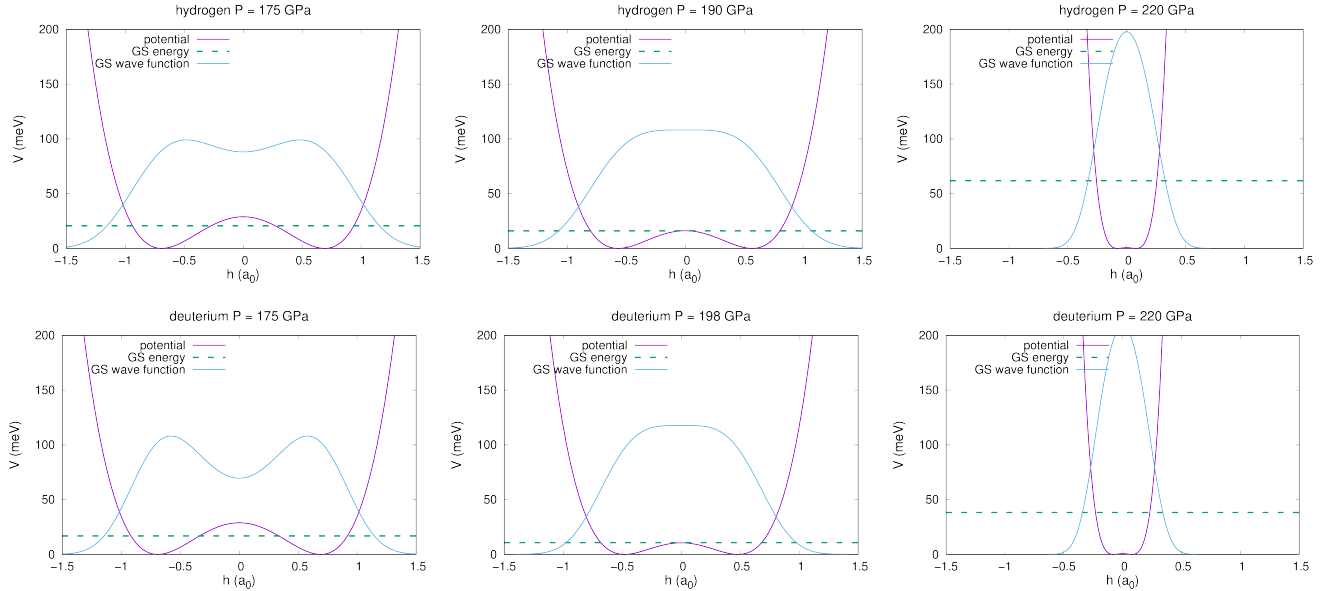


Figure 13. Potential (violet line), GS wave function (cyan line) and GS energy (dashed green line) for the hydrogen (upper row) and deuterium (lower row) librational degrees of freedom, as a function of the order parameter h , for a system with $N_{\text{mol}} = 4$ canted dimers per unit cell of 12 molecules. The central column is computed at the transition pressure p_c separating phase II and III, while the left (right)-hand side column is for $p = 175$ GPa ($p = 220$ GPa), deep in phase II (phase III).

of 4 molecules each, one with the largest h , the second with an intermediate value, the last one with the smallest out-of-plane component. Solving Eq. 6 with $N_{\text{mol}} = 4$ and $N_{\text{mol}} = 8$ yields an estimate of the p_c range. Two conclusions can be drawn from this analysis:

- the estimated isotopic effect across the II-III phase boundary amounts approximately to 10 GPa;
- in hydrogen, the NQEs shift due to the librational degrees of freedom is ≈ 25 GPa from the static lattice pressure toward lower values.

BADER ANALYSIS AND INFRARED SPECTRA

Below we present the results from the Bader analyses of C2/c-24 and P-1-24. The structures are visualized from two perspectives in Fig. 10. In Fig. 14 we plot the polarization as function pressure for the six inequivalent molecules in P-1-24. After the transition there are three inequivalent molecules that lie in plane and the symmetry increases to C2/c. At the same time the polarization increases. A similar analysis was performed in Ref. [28] for C2/c-24 and P6₃/m-16.

In Fig. 15 we plot the infrared (IR) intensity of the IR active vibron modes at different pressures. Comparing to the experimental results of Ref. [6] we see a very similar behavior.

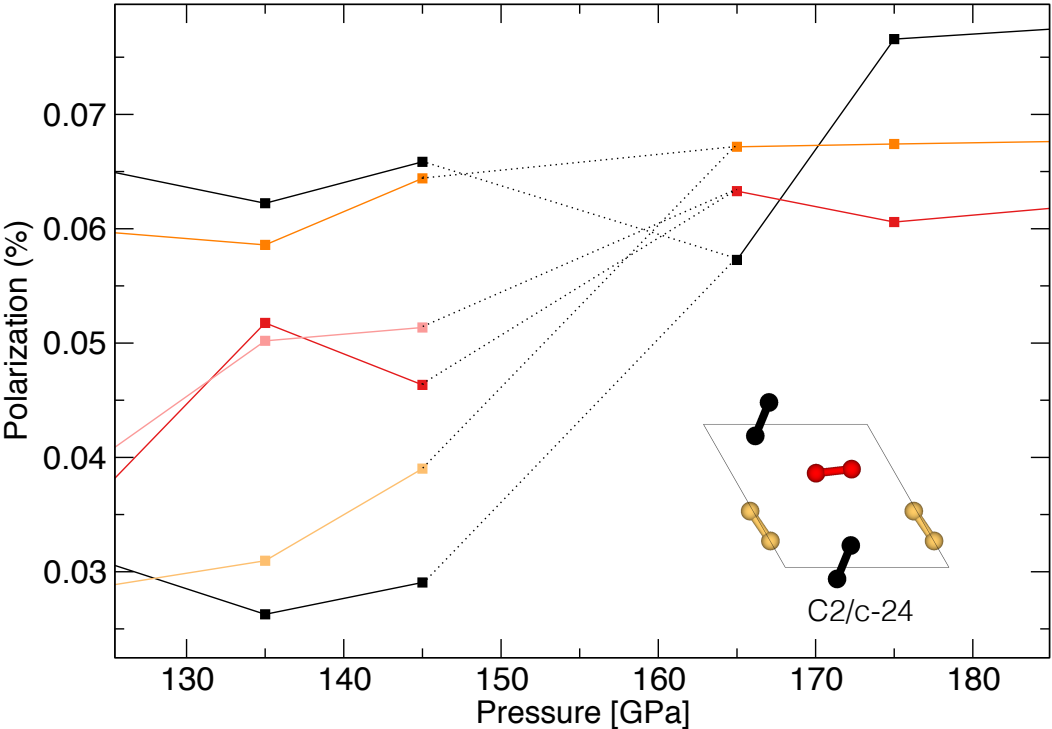


Figure 14. The polarization of the molecular units in C2/c-24 and P-1-24 obtained with a Bader analysis. While there are three inequivalent molecules in C2/c-24 there are six in P-1-24. The inset shows a single layer of C2/c-24 where the molecules are colored by their polarization in the main figure.

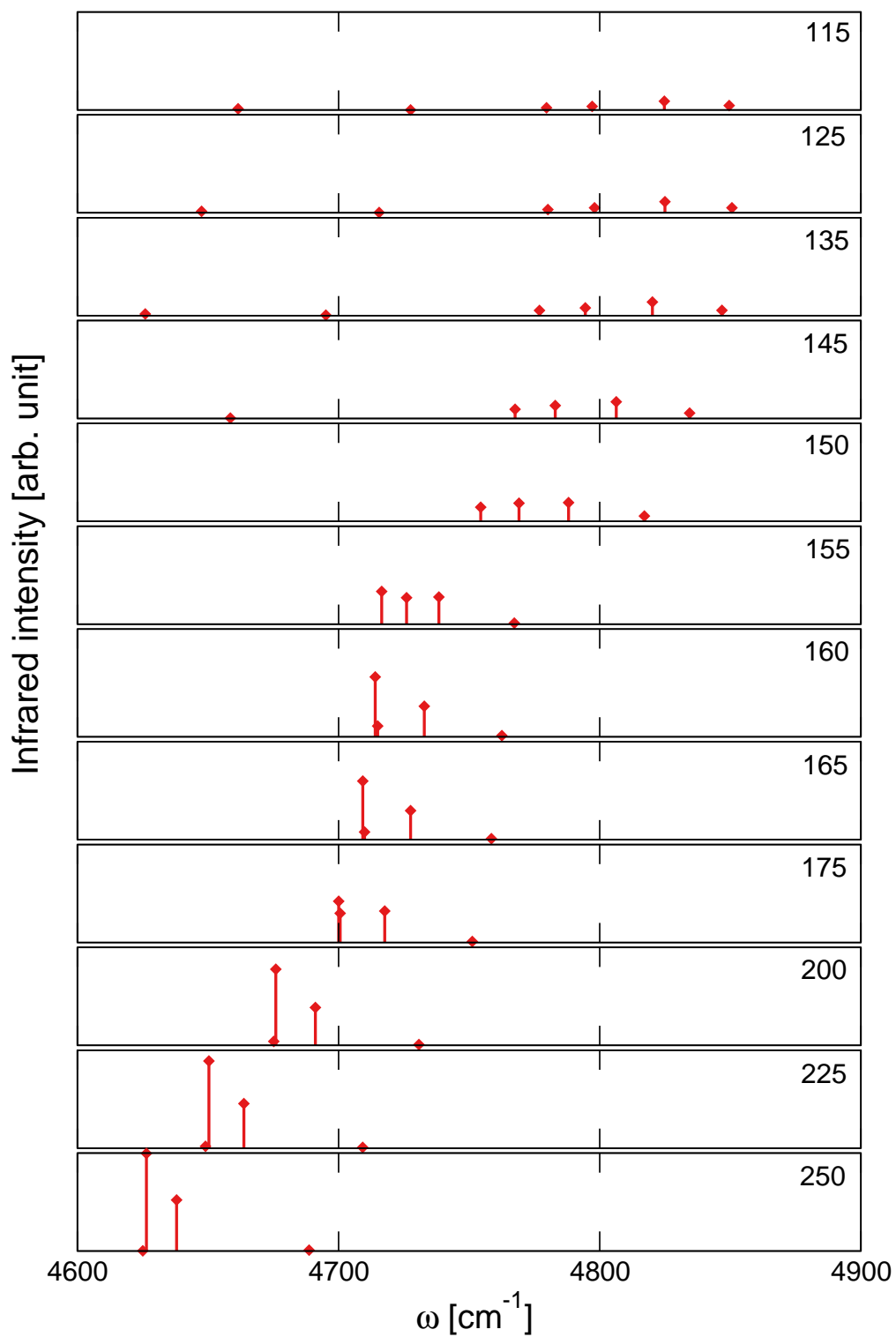


Figure 15. The intensity of the infrared active vibrons as a function of pressure for C2/c-24. At approximately 155 GPa the C2/c-24 phase turns into P-1-24, signaled by the frequency shift and increase in intensity.